



# High-throughput and label-free parasitemia quantification and stage differentiation for malaria-infected red blood cells

Xiaonan Yang<sup>a,b</sup>, Zhuofa Chen<sup>a</sup>, Jun Miao<sup>c</sup>, Liwang Cui<sup>c</sup>, Weihua Guan<sup>a,d,\*</sup>

<sup>a</sup> Department of Electrical Engineering, Pennsylvania State University, University Park 16802, USA

<sup>b</sup> School of Information Engineering, Zhengzhou University, Zhengzhou 450000, China

<sup>c</sup> Department of Entomology, Pennsylvania State University, University Park 16802, USA

<sup>d</sup> Department of Biomedical Engineering, Pennsylvania State University, University Park 16802, USA

## ARTICLE INFO

### Keywords:

Cell deformability  
Single cell  
Malaria  
Microfluidics  
Parasitemia quantification

## ABSTRACT

This work reports a high throughput and label-free microfluidic cell deformability sensor for quantitative parasitemia measurement and stage determination for *Plasmodium falciparum*-infected red blood cells (*Pf*-iRBCs). The sensor relies on differentiating the RBC deformability (a mechanical biomarker) that is highly correlated with the infection status. The cell deformability is measured by evaluating the transit time when each individual RBC squeezes through a microscale constriction (cross-section  $\sim 5 \mu\text{m} \times 5 \mu\text{m}$ ). More than 30,000 RBCs can be analyzed for parasitemia quantification in under 1 min with a throughput  $\sim 500$  cells/s. Moreover, the device can also differentiate various malaria stages (ring, trophozoite, and schizont stage) due to their varied deformability. Using *Pf*-iRBCs at 0.1% parasitemia as a testing sample, the microfluidic deformability sensor achieved an excellent sensitivity (94.29%), specificity (86.67%) and accuracy (92.00%) in a blind test, comparable to the gold standard of the blood smear microscopy. As a supplement technology to the microscopy and flow cytometry, the microfluidic deformability sensor would possibly allow for label-free, rapid and cost-effective parasitemia quantification and stage determination for malaria in remote regions.

## 1. Introduction

Malaria is one of the most prevalent infectious diseases for which almost half of the global population is at risk (Alves-Junior et al., 2014; Enayati and Hemingway, 2010; Greenwood and Mutabingwa, 2002; Bhatt et al., 2015). According to the world malaria report, more than 212 million people suffer from malaria infections, and over 400 thousand people died from this preventable disease each year (Alves-Junior et al., 2014). Parasitemia is a critical parameter for quantifying the parasite load in the organism and indicates the degree of an active parasitic infection (Hopkins et al., 2013; Molineaux et al., 2001). Quantitative measurement of parasitemia and stage determination is important in many phases of malaria assessment, such as the diagnosis and the therapy follow-up, particularly in the chronic phase (Bianco et al., 1986). The microscopy based morphology analysis still remains the gold standard for parasitemia quantification. The advantages of microscopy are several folds: it is possible to differentiate between species, quantify parasitemia with high sensitivity (0.001%) and observe asexual stages of the parasites (Ross et al., 2006; Yager et al., 2006). Nevertheless, the microscopy method has several drawbacks, including the reliance of an expert reading Giemsa-stained blood

smears, subjectivity, low reproducibility and relatively low speed ( $> 5$  mins/slide) (Prescott et al., 2012). The flow cytometry could offer higher sensitivity and overcome the speed limitation of the microscopy. However, the high cost of the instrumentation and the labeling process limits its widespread usage (Bei et al., 2010; Makler et al., 1998). In addition, both microscopy and flow cytometry require time-consuming staining or labeling processes. It is highly desirable to develop a label-free technology for parasitemia quantification. To that end, Peng et al. recently reported a micromagnetic resonance relaxometry (MRR) based label-free platform for parasitemia quantification in whole blood (Peng et al., 2014; Karl et al., 2015). This method detects the variation in spin-spin relaxation time of MRR signals from paramagnetic hemozoin particles with a bulk measurement.

It is well known that *Plasmodium falciparum*-infected red blood cells (*Pf*-iRBCs) become increasingly rigid (less deformable) as they mature (Hou et al., 2010), thus the deformability has the potential to be used as a mechanical biomarker to distinguish the healthy and the infected RBCs at various stages (Kang et al., 2016). To date, various microfluidic-based methods have been developed to interrogate the cell deformability. For example, hydrodynamic pressure-based interrogation (e.g., inertial microfluidics (Gossett et al., 2012; Cha et al., 2012;

\* Corresponding author at: Department of Electrical Engineering, Pennsylvania State University, University Park 16802, USA.  
E-mail address: [w.guan@psu.edu](mailto:w.guan@psu.edu) (W. Guan).

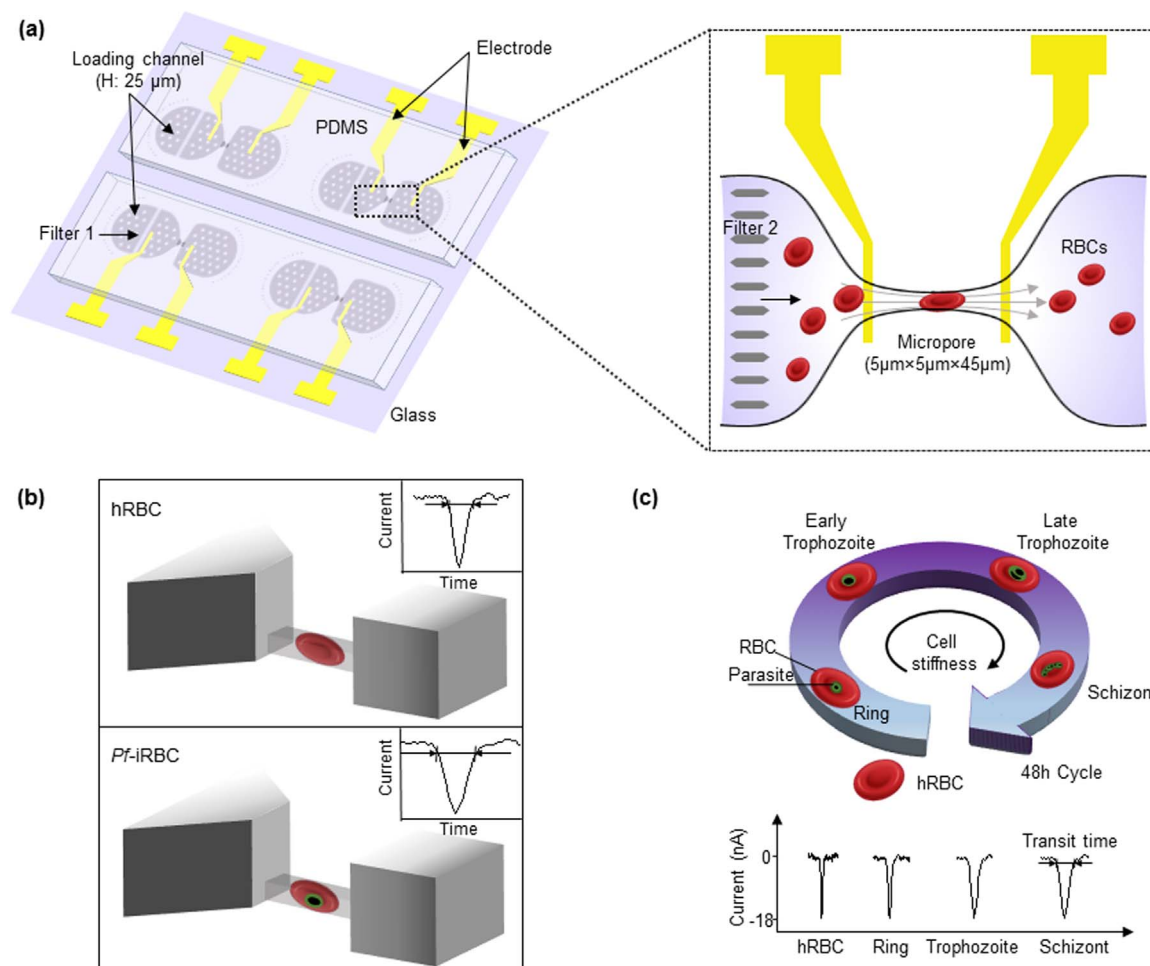


**Fig. 1.** Overview of the label-free microfluidic cell deformability sensor. (a) Schematic of the deformability sensor for highly-throughput and label-free parasitemia quantification. (b) The principle of the deformability sensor to differentiate hRBCs and *Pf*-iRBCs. When an RBC squeezes through the micropore, an ionic current dip occurs due to the reduced conduction cross-section. The cell translocation time is determined by the cell deformability. (c) The stiffness of the red blood cells increases monotonically as *P. falciparum* parasites evolving from ring stage to the trophozoite and finally to the schizont stage. The deformability sensor could thus differentiate malaria at different stages.

Dudani et al., 2013; Tse et al., 2013), and real-time deformability cytometry (Otto et al., 2015)), and physical constraint-based interrogation (e.g., single micropore (Faustino et al., 2014; Song et al., 2013) and microchannel (Zheng et al., 2012; Du et al., 2013; Guan et al., 2012; Wan et al., 2008), and arrayed microchannels (Guo et al., 2012; Zhang et al., 2012; Rosenbluth et al., 2008; Huang et al., 2013; Lange et al., 2015; Herricks et al., 2009; Liu et al., 2015)). Despite success in the qualitative characterization of *Pf*-iRBCs deformability properties, a high throughput quantitative parasitemia measurement at the single cell level has yet to be developed.

In this work, we demonstrated a label-free microfluidic cell deformability sensor for quantitative and high-throughput parasitemia measurement and stage determination for *Pf*-iRBCs. The deformability sensor is capable of analyzing more than 30,000 RBCs within 1 min (throughput ~ 500 cells/s). Moreover, the device is able to differentiate various malaria stages among ring, trophozoite, and schizont stage. With 0.1% *Pf*-iRBCs as a testing sample, the microfluidic deformability sensor achieved an excellent sensitivity (94.29%), specificity (86.67%) and accuracy (92.00%) in a blind test, comparable to the gold standard of the blood smear microscopy. With minimal manual work, the microfluidic deformability sensor could deliver sensitive and accurate parasitemia measurement directly from a small volume of blood samples within a few minutes, which is highly promising for sensitive malaria diagnosis in field settings.

## 2. Materials and methods

### 2.1. *P. falciparum* culture and sample preparation

The *P. falciparum* 3D7 was cultured in type O<sup>+</sup> human red blood cells in RPMI 1640 medium supplemented with 25 mM HEPES, 50 mg/L hypoxanthine, 25 mM NaHCO<sub>3</sub>, and 0.5% AlbuMix (Thomas Scientific, U.S.A). The parasite culture was synchronized by treatment of ring-stage parasites with 5% D-sorbitol. The parasites were taken at 2 h, 18 h, and 32 h post synchronization to represent the ring, trophozoite, and schizont as determined by microscopy. The cultured *P. falciparum* sample prior to electrical sensing measurement consisted of a mixture of *Pf*-iRBCs and uninfected RBCs at a parasitemia of ~3%. In all electrical measurements, 30 μL blood was diluted in 1 mL buffer solution consists of phosphate buffer saline (PBS; Thomas Scientific, U.S.A) and 1% w/v Bovine Serum Albumin (BSA; Sigma-Aldrich, Canada).

### 2.2. Thin smear microscopy

Parasitemia was examined by Giemsa staining. A drop of parasite culture was smeared on a glass slide, dried at room temperature, fixed with methanol for 10 s, and stained with Giemsa working solution for 10 min. The slide was then rinsed briefly in tap water, dried and examined under a microscope. Parasitemia was determined by count-

ing at least 1000 RBCs under a microscope, equipped with a 100× oil-immersion objective.

### 2.3. Microfluidic device fabrication

The cell deformability sensor was designed in a layout editor and printed on a transparent mask. The casting mold was fabricated by a standard double layer lithography process on a 4-in. silicon wafer (Zheng et al., 2013). The microfluidic chips were made of polydimethylsiloxane (PDMS) by casting onto the SU8 mold. It consists of two layers with different thicknesses: micropore area with ~5 μm and loading channel area with ~25 μm, respectively. The loading channel's cross-sectional area (1000×25 μm<sup>2</sup>) is much larger than that of the micropore to reduce the hydrodynamic and the electrical resistance. The micropore size needs to be small enough for improved time resolution but also large enough for avoiding the micropore clogging by cells. We found 5 μm is the optimized size for the experiments. The length of the micropore (~45 μm) also needs to be optimized. A longer channel makes the cell transit time longer, amplifying the differences between cells and making the device more sensitive. On the other hand, a longer channel increases the risk of clogging. To avoid the micropore clogging by cell aggregates and debris, we have incorporated two stages of filters on the microfluidic chip (filter 1 in the loading channel area and filter 2 in the micropore area, Fig. 1a).

The Au/Cr electrodes (20 nm adhesive Cr layer and 80 nm Au layer) were evaporated on a cover glass (thickness ~ 130 μm, Ted Pella) through a laser machined Polymethylmethacrylate (PMMA) shadow mask. To enhance the signal-to-noise ratio, the microelectrodes were positioned close to the micropore area. The PDMS replica was permanently bonded to the cover glass through oxygen plasma treatment.

### 2.4. Electrical measurement and data analysis

After device fabrication, the microfluidic chip was housed inside a home-made Faraday cage to shield the environment noise. A constant voltage (~ 600 mV) was applied across the micropore constriction. The polarity of the applied voltage was switched periodically to avoid severe electrode damage due to possible electrochemical reactions. The ionic current was monitored as each single individual RBC translocating through the micropore. An adjustable pressure source was used to drive the cells on the microfluidic chip. Since the buffer solution (1x PBS) were constantly flowing during the experiments, the accumulation of the electroactive species near the electrode is very unlikely to interfere with the ionic current measurement. The ionic current traces were recorded by an amplifier (Axopatch 200B, Molecular Devices, U.S.A). The analog output of the amplifier was sampled with 16-bit DAQ card (NI PCI-6363, National Instruments, U.S.A) and a data acquisition software (LabVIEW). The sampling rate for the measurement was 100 kHz. A custom-built MATLAB (MathWorks) program was developed to analyze the data off-line. The transit time was extracted from each individual cell when translocating the micropore.

## 3. Results and discussion

### 3.1. Sensing principle

Fig. 1a shows the schematic and the principle of the microfluidic deformability sensor. The corresponding equivalent circuit model is presented in Supplementary Information (Fig. S1). The electrical resistance of the deformability sensor is mainly dominated by the micropore constriction due to the cross-sectional dimension ratio between the micropore and the loading channel. When an RBC squeezes through the micropore, an ionic current dip occurs as a result of the reduced conduction cross-section. In a typical experiment, a pressure of 1–1.5 psi is applied, corresponding to a flow rate of ~180 μm/ms.

Since the micropore has a slightly smaller size than that of the RBCs (diameter ~7 μm), RBCs have to squeeze through the micropore. The cell transit time is a complex function of various parameters: the applied pressure, the cell size, the cell deformability, the micropore size, and the PDMS and cell surface properties etc. (Nyberg et al., 2016; Shelby et al., 2003). These parameters except the cell deformability were controlled to remain the same for a given experimental setup. Therefore, the transit time is an indirect measurement for the cell deformability alone. In other words, the rigid *Pf*-iRBCs will spend more time (on average) squeezing through the micro-constriction than the more deformable healthy RBCs (hRBCs) (Fig. 1b).

In the intraerythrocytic cycle, the *P. falciparum* parasites evolve from ring stage to the trophozoite and finally to the schizont stage (Fig. 1c). During this process, the stiffness of the cells increases monotonically from 8 μN/m to 16 μN/m at ring stage and finally to 53 μN/m at schizont stage (Hou et al., 2010; Mills et al., 2007; Park et al., 2008). Therefore, the transit time of the *Pf*-iRBCs is also expected to increase as parasites develop into late stages (Fig. 1c). The *Pf*-iRBCs deformability variations among various stages could thus be utilized for malaria stages differentiation.

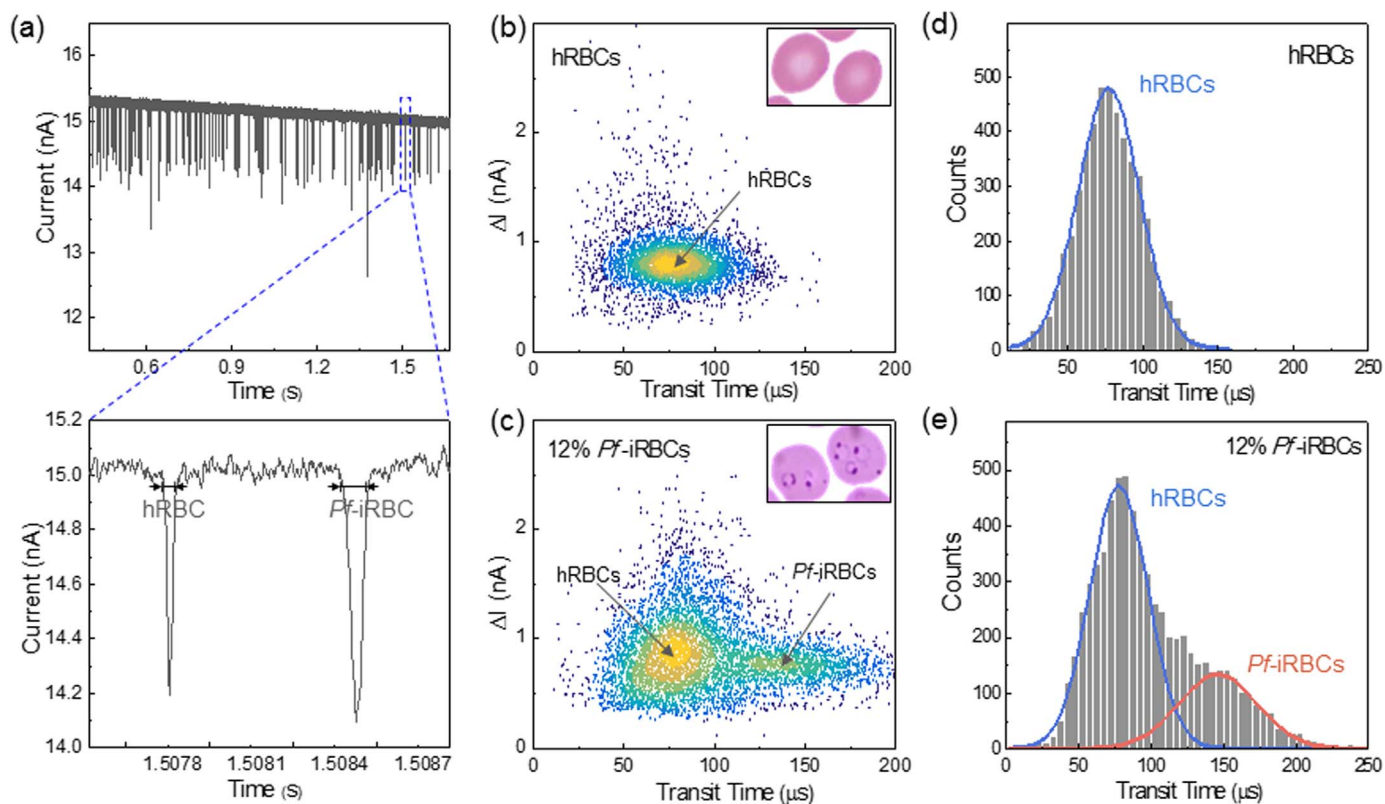
We can model the total time distribution data as a mixture consisting of maximal *k* populations (healthy, ring, trophozoites and schizonts). Each of these populations can be assumed as a Gaussian distribution  $N(\mu, \sigma)$ . As a result, the mixture distribution of the transit time can be represented by summing the Gaussian distribution function  $t = \sum_{i=1}^k \alpha_i N(\mu_i, \sigma_i)$  with the constraint of  $\sum_{i=1}^k \alpha_i = 1$ . The weight  $\alpha_i$  represents the population percentage for each population, which can be fitted by using expectation maximization (EM) algorithm.

### 3.2. Differentiate ring stage *Pf*-iRBCs and hRBCs

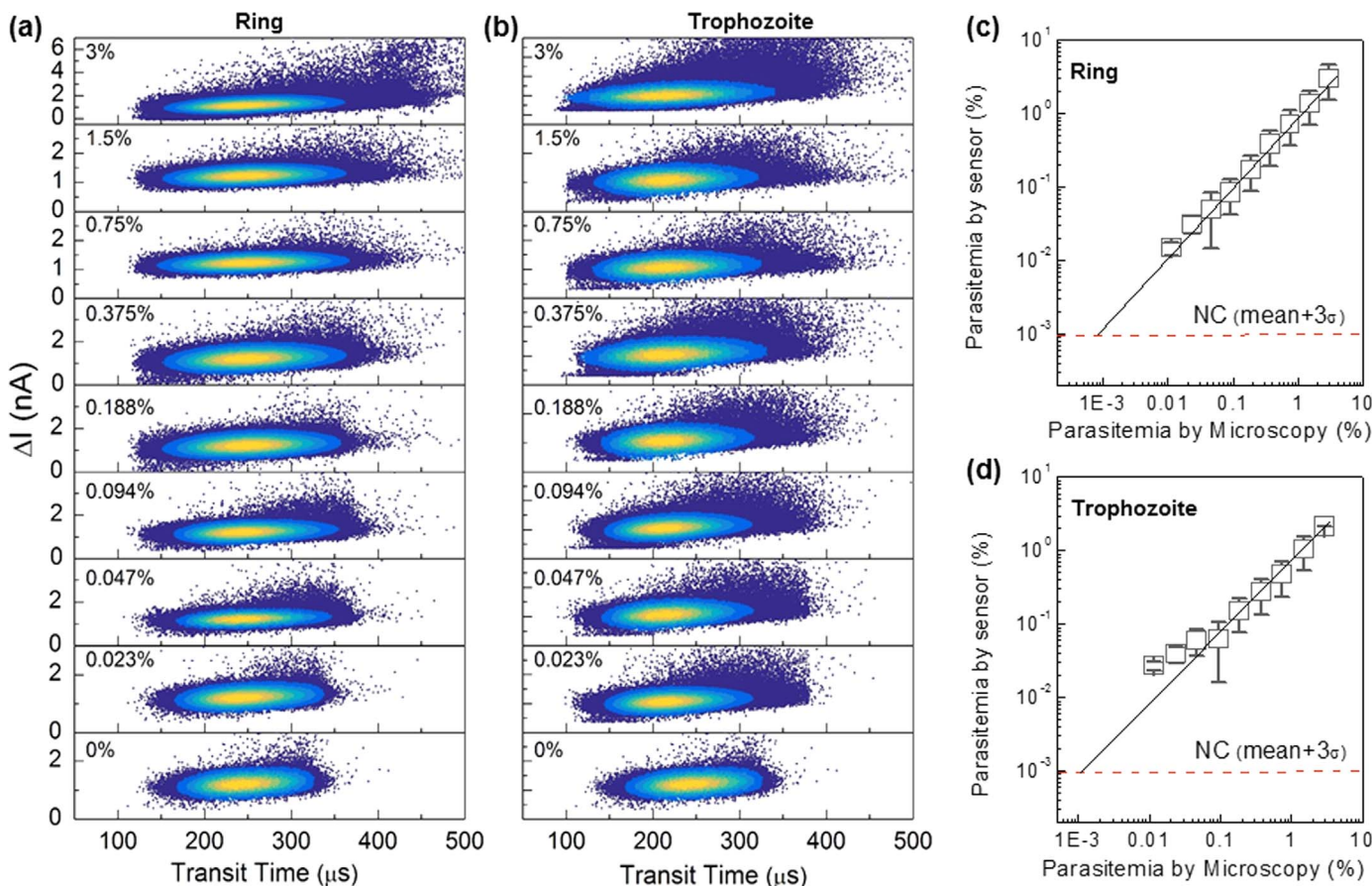
Before testing with the RBCs, the microfluidic deformability sensor and the testing apparatus was validated by the measurements of a mixture of polystyrene microbeads with diameters of 5 μm and 10 μm (with a concentration of  $1 \times 10^5$ /mL and  $3 \times 10^4$ /mL, respectively. Fig. S2). After that, the ring stage *Pf*-iRBCs at 12% parasitemia and the control hRBC samples were tested. Fig. 2a shows a typical current trace, where the transit time and the current dip for each single cell can be extracted.

Fig. 2b shows the scattering plot of the transit time and ionic current dip for the 100% hRBC sample, while Fig. 2c shows the case for the sample at 12% parasitemia (i.e., ~12% *Pf*-iRBCs and ~88% hRBCs). Both hRBCs and *Pf*-iRBCs deformed when squeezing through the micropore constriction under the same experimental conditions (i.e., same flow rate, voltage bias, sampling rate and the device conditions). As the cells passing through the micropore constriction, we tracked their size and transit time by evaluating the amplitude and width of the ionic current dip, respectively. As shown in Fig. 2c, a clear separate population appears for the 12% parasitemia sample as compared to the hRBC sample shown in Fig. 2b. This additional population has a longer cell transit time than the hRBC population.

Fig. 2d and e plot the transit time histogram for the control hRBC sample and the 12% *Pf*-iRBCs sample. The transit time for the control hRBC sample shows a normal distribution (Fig. 2d). The correlation coefficient of the Gaussian fitting curve is  $R^2=99.1\%$ , indicating that the normal distributions provide a good description of the measured data. The 12% *Pf*-iRBCs sample shows two peaks in the normal plot on the cell transit time distribution, with mean values of  $78 \pm 20.4 \mu\text{s}$  (hRBC population) and  $155 \pm 24.8 \mu\text{s}$  (*Pf*-iRBC population) (Fig. 2e). This is consistent with the hypothesis that cell deformability is a determining factor for cell transit time across the micropore constriction. The differentiating ability of the microfluidic deformability sensor can be evaluated based on a parameter given by (Zheng et al., 2013),  $R_s = (\mu_1 - \mu_2) / \sqrt{\sigma_1^2 + \sigma_2^2}$ , where  $\mu_1, \mu_2$ , are the mean value and  $\sigma_1, \sigma_2$  denote the standard deviation of transit time for two groups. It is



**Fig. 2.** (a) The current trace for *Pf*-iRBC sample at 12% parasitemia. The scattering plot of transit time and ionic current dip for (b) pure RBC sample and (c) *Pf*-iRBC sample at 12% parasitemia. Histogram plot of cell transit time for (d) pure RBC sample and (e) *Pf*-iRBC sample at 12% parasitemia.



**Fig. 3.** Scattering plot of transit time versus ionic current dip for the *Pf*-RBCs with various parasitemia for (a) ring and (b) trophozoite *Pf*-iRBC. Corresponding parasitemia determined by the microfluidic deformability sensor and the microscopy method for (c) ring and (d) trophozoite *Pf*-iRBC.

noteworthy that different applied pressure will lead to an overall transit time shift for each population ( $\mu_1$  and  $\mu_2$ ). Nevertheless, the difference of the mean transit time ( $\mu_1 - \mu_2$ ) is independent of the flow rate.

### 3.3. Parasitemia quantification at ring and trophozoite stages

The microfluidic cell deformability sensor can not only differentiate ring stage *Pf*-iRBCs and hRBCs but can also quantify the parasitemia. Parasitemia ranging from 0.023% to 3% were prepared with  $2\times$  serial dilution of *Pf*-iRBCs samples of cultured asexual parasites with known parasitemia. These samples were tested under the same experimental conditions.

Fig. 3a and b show the scattering plot of the transit time and current dip for the ring and trophozoite *Pf*-iRBCs samples, respectively. A decreasing cell population of larger transit time was clearly observed when sample parasitemia was reduced. This trend is clear for both the ring and the trophozoite samples. Fig. 3c and d show the parasitemia determined by the microfluidic deformability sensor *versus* the parasitemia determined by the thin smear microscopy for ring and trophozoite *Pf*-iRBCs, respectively. Remarkably, there was an excellent linear relationship ( $R^2 > 98\%$ ) between the parasitemia determined by deformability sensor and microscopy, both for ring and trophozoite stages. The agreement between these two methods validates the parasitemia quantification ability of the microfluidic deformability sensor. It is noteworthy that the microfluidic deformability sensor can analyze more than 30,000 RBCs within 1 min, a much higher throughput than that of the microscopy method ( $\sim 5$  min/slide).

It is also interesting to compare the transit time of ring and trophozoite stages at the same parasitemia (Fig. 3a and b). Note that each of the two samples would have a common healthy RBC population and a stage-specific population. For the common healthy RBC population, we would expect the same transit time distribution while for the stage-specific population, a right shift of the trophozoite transit time would be expected since trophozoite parasites are stiffer than ring parasites. Although experiment-to-experiment variations (device size, and pressure etc.) can lead to an overall shift in the transit time distribution, the healthy population could be used as the reference to infer the relative population transit time difference for the two stages (Supplementary Information, Fig. S3).

### 3.4. Parasite evolution in an intraerythrocytic cycle

In the intraerythrocytic cycle, the stiffness of the *Pf*-iRBCs increases monotonically from the ring stage to the schizont stage. To evaluate the sensor's stability to monitor the stiffness change during an intraerythrocytic cycle, the hRBCs were firstly infected with 2% *P. falciparum* parasites at time zero. The infected RBC was then continuously monitored (interval of 5–8 h) for a typical intraerythrocytic cycle ( $\sim 48$  h). The deformability and the parasitemia evolution was analyzed by the microfluidic deformability sensor, benchmarked with the reference method of thin smear microscopy.

Fig. 4a shows the scattering plot of the transit time and current dip of the monitored sample in a typical intraerythrocytic cycle. A clear right-shift of the transit time can be observed from 0 h to 48 h, corresponding to the parasite evolution from ring stage and to the late stage of trophozoite and schizont. This observation is consistent with the fact that *Pf*-iRBCs become stiffer as parasites develop into late stages. The result suggests the deformability could be used as a potential mechanical biomarker to differentiate malaria at different stages. It is noteworthy that the parasite evolution in an intraerythrocytic cycle is asynchronous. Therefore, the infected population is of a mixed nature at a specific time spot. A clear turning pointing from one stage to the other does not exist.

Fig. 4b shows the parasitemia quantified by the deformability sensor and the thin smear microscopy during the intraerythrocytic cycles. The parasitemia determined by the two methods agrees with each other very well. This can also be clearly seen from Fig. 4c. A linear relationship between the parasitemia determined by both methods ( $R^2 > 96\%$ ) further confirms the reliability of deformability sensor in parasitemia quantification. It is very interesting to note that the parasitemia standard deviation is less in deformability sensors than that in the thin smear microscopy (Fig. 4b). This is due to the fact that the deformability sensors can examine a lot more cells than the microscopy method. An increased sample size can reduce the statistical variations. In addition, both methods confirm a gradual parasitemia increase before reaching  $\sim 2\%$  level at the time of 48 h. This is attributed to the fact that parasites evolution during the intraerythrocytic cycles is asynchronous (Cowman and Crabb, 2006).

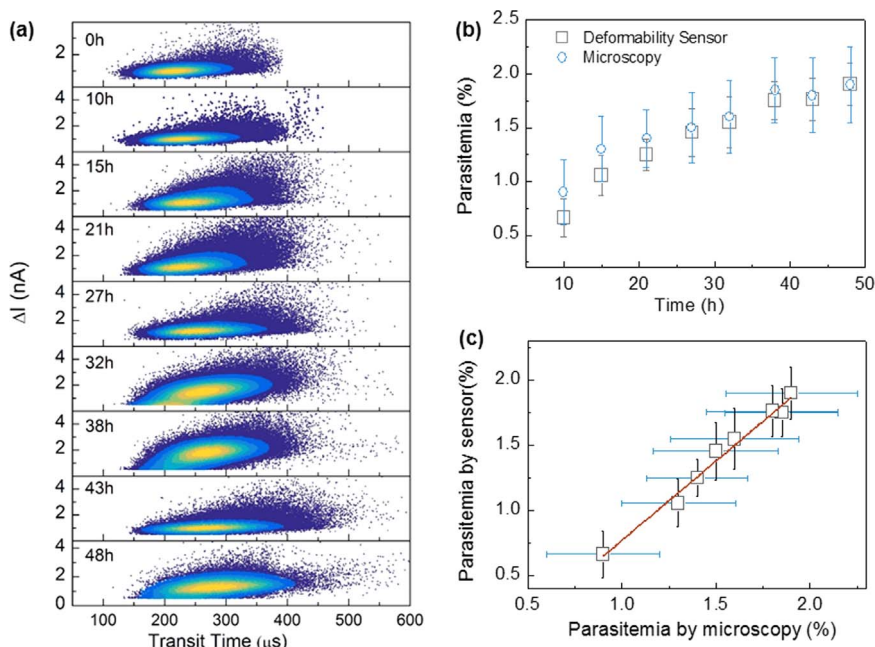


**Fig. 4.** The analysis for the *Pf*-iRBCs at different stages during the intraerythrocytic cycles. (a) Scattering plot of transit time *versus* ionic current dip for the *Pf*-iRBC during the intraerythrocytic cycle at various time spots. (b) The parasitemia quantified by the deformability sensor and microscope during the intraerythrocytic cycles. (c) Comparison of parasitemia between the deformability sensor and the microscope.

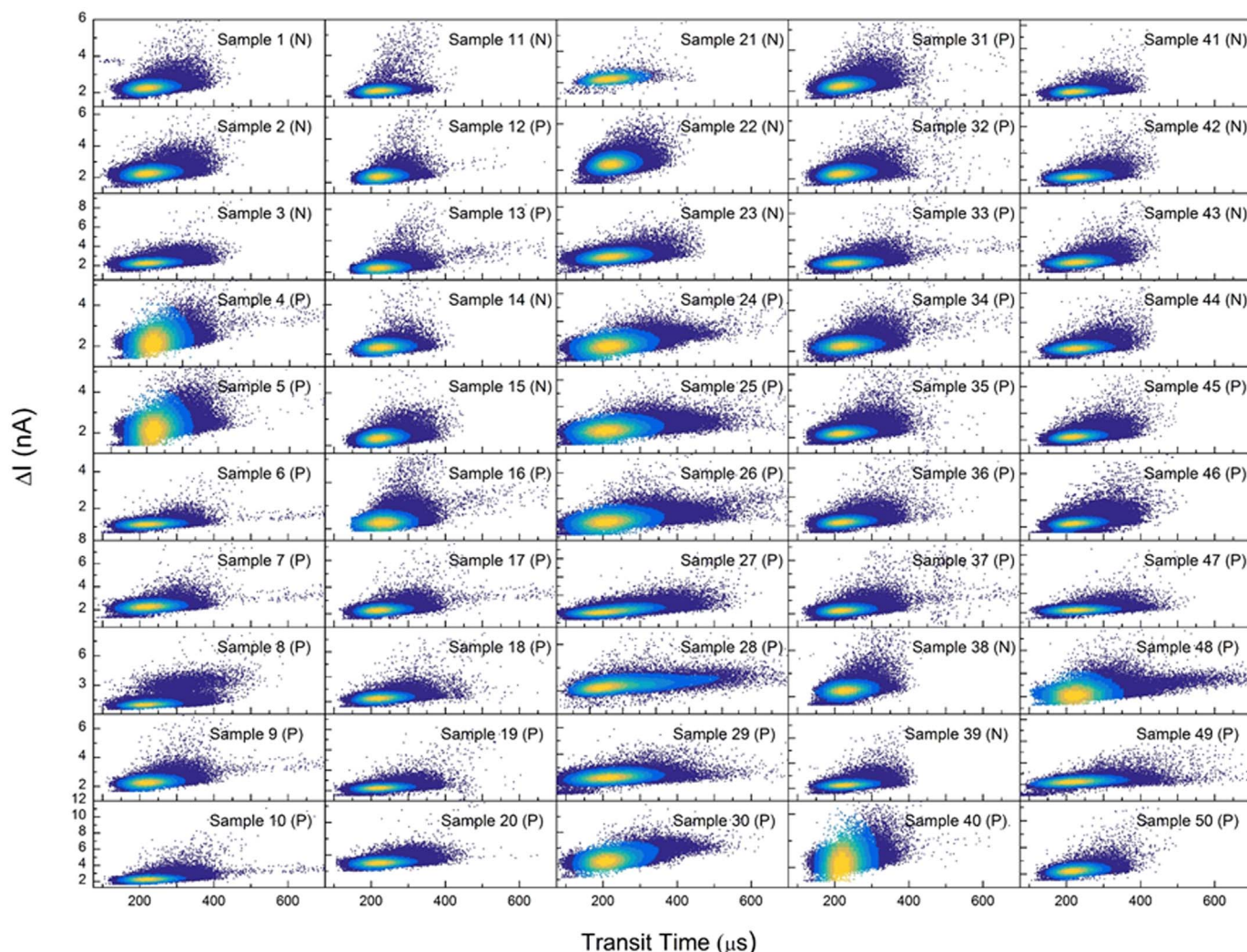


Fig. 5. The scattering plot of the transit time and current dip for the 50 samples in the blind test.

### 3.5. Blind test with *Pf*-iRBCs at 0.1% parasitemia

In order to evaluate the use of the microfluidic deformability sensor for qualitative positive/negative diagnosis, we performed a blind study on the deformability sensor with traditional microscopy method as the reference. We infected hRBCs with *P. falciparum* at a percentage of 0.1% for a total of 50 samples. The *P. falciparum* was at different stages ranging from the ring stage to the schizont stage. The infectious status of each sample was recorded but kept blind to the technicians. We asked three technicians with experienced microscopic skills and a technician well-trained with microfluidic deformability sensor to independently make a positive/negative call. The measured scattering plot of the transit time and current dip for these 50 samples from the deformability sensor were described in Fig. 5. The sample was deemed as positive in the microfluidic deformability sensor when the cell number larger than the threshold transit time is over 100 (this process was automated by the software). Otherwise, it was regarded as negative. At the end of the blind experiment, the results were checked against the recorded information to determine the rate for true positive, true negative, false positive and false negative (Supplementary Table S1). Table 1 shows the statistical summary of the blind test. The microfluidic deformability sensor achieved an excellent sensitivity (94.29%), specificity (86.67%) and accuracy (92.00%) in a blind test. This is comparable to the gold standard of the blood smear microscopy (sensitivity of 95.21%, specificity of 89.17% and accuracy of 92%).

Table 1

A summary of the overall performance of deformability sensor as compared to the blood smear microscopy in the blind test. The variables measured were the number of true positives (TP), number of true negatives (TN), number of false positives (FP) and number of false negatives (FN). Sensitivity was calculated as TP/(TP + FN), specificity was calculated as TN/(TN + FP) and test accuracy is defined as (TP + TN)/(TP + TN + FP + FN).

Test parameters	Microfluidic Sensor	Microscopy				
		T1	T2	T3	Mean	Std. dev.
True positive, TP	33	34	33	32	33.0	1.00
True negative, TN	13	14	14	13	13.7	0.580
False positive, FP	2	1	2	2	1.67	0.580
False negative, FN	2	1	1	3	1.67	1.15
Sensitivity	94.3%	97.1%	97.1%	91.4%	95.2%	3.28%
Specificity	86.7%	93.3%	87.5%	86.7%	89.2%	3.63%
Test accuracy	92.0%	96.0%	94.0%	90.0%	93.3%	3.06%

## 4. Conclusion

Using the unique cell deformability property as the mechanical biomarker, a high throughput and label-free microfluidic deformability sensor was developed and demonstrated for potential cost-effective

malaria diagnosis. We have shown the parasitemia measurement can be rapidly quantified (< 1 min) by evaluating the deformability of each single cells in a large population (> 30 k) passing through the microscale constrict. We have also shown that the malaria infectious stage information can be derived by using a Gaussian mixture model. In addition, the practical usage of the device is validated in a blind qualitative positive/negative test. The device has shown a high sensitivity (94.29%), specificity (86.67%) and accuracy (92.00%) in the blind test. For the current device, the removal of the white blood cells (WBCs) is essential. Future works to filter the WBCs on the chip and to integrate the peripheral electronics and the pressure sources would be important towards the final goal of clinical usage.

## Acknowledgments

This project was partly supported by the Penn State CTSI Grant (UL Tr000127) from the National Center for Advancing Translational Sciences, National Institutes of Health. The content is solely the responsibility of the authors and does not necessarily represent the official views of the NIH. This project was also supported by Penn State ENGINEering for Innovation & ENtrepreneurship (ENGINE) Grant.

## Appendix A. Supporting information

Supplementary data associated with this article can be found in the online version at doi:10.1016/j.bios.2017.07.019.

## References

- Alves-Junior, E.R., Gomes, L.T., Assis-Oliveira, F.B., Silverio-Silva, L.R., Nery, A.F., Fontes, C.J., 2014. *Trop. Biomed.* 31, 387–391.
- Bei, A.K., DeSimone, T.M., Badiane, A.S., Ahouidi, A.D., Dieye, T., Ndiaye, D., Sarr, O., Ndir, O., Mboup, S., Duraisingh, M.T., 2010. *Am. J. Hematol.* 85, 234–237.
- Bhatt, S., Weiss, D.J., Cameron, E., Bisanzio, D., Mappin, B., Dalrymple, U., Battle, K.E., Moyes, C.L., Henry, A., Eckhoff, P.A., Wenger, E.A., Briet, O., Penny, M.A., Smith, T.A., Bennett, A., Yukich, J., Eisele, T.P., Griffin, J.T., Fergus, C.A., Lynch, M., Lindgren, F., Cohen, J.M., Murray, C.L.J., Smith, D.L., Hay, S.I., Cibulskis, R.E., Gething, P.W., 2015. *Nature* 526, 207–211.
- Bianco, A.E., Battye, F.L., Brown, G.V., 1986. *Exp. Parasitol.* 62, 275–282.
- Cha, S., Shin, T., Lee, S.S., Shim, W., Lee, G., Lee, S.J., Kim, Y., Kim, J.M., 2012. *Anal. Chem.* 84, 10471–10477.
- Cowman, A.F., Crabb, B.S., 2006. *Cell* 124, 755–766.
- Du, E., Ha, S., Diez-Silva, M., Dao, M., Suresh, S., Chandrakasan, A.P., 2013. *Lab a Chip* 13, 3903–3909.
- Dudani, J.S., Gossett, D.R., Tse, H.T.K., Di Carlo, D., 2013. *Lab Chip* 13, 3728–3734.
- Enayati, A., Hemingway, J., 2010. *Annu. Rev. Entomol.* 55, 569–591.
- Faustino, V., Pinho, D., Yaginuma, T., Calhelha, R.C., Ferreira, I.C.F.R., Lima, R., 2014. *Biochip J.* 8, 42–47.
- Gossett, D.R., Tse, H.T.K., Lee, S.A., Ying, Y., Lindgren, A.G., Yang, O.O., Rao, J.Y., Clark, A.T., Di Carlo, D., 2012. *P Natl. Acad. Sci. USA* 109, 7630–7635.
- Greenwood, B., Mutabingwa, T., 2002. *Nature* 415, 670–672.
- Guan, G.F., Chen, P.C.Y., Peng, W.K., Bhagat, A.A., Ong, C.J., Han, J.Y., 2012. *J. Micromech. Microeng.*, 22.
- Guo, Q., Reiling, S.J., Rohrbach, P., Ma, H.S., 2012. *Lab a Chip* 12, 1143–1150.
- Herrick, T., Antia, M., Rathod, P.K., 2009. *Cell Microbiol* 11, 1340–1353.
- Hopkins, H., Gonzalez, L.J., Polley, S.D., Angutoko, P., Ategeka, J., Asiimwe, C., Agaba, B., Kyabayinze, D.J., Sutherland, C.J., Perkins, M.D., Bell, D., 2013. *J. Infect. Dis.* 208, 645–652.
- Hou, H.W., Bhagat, A.A.S., Chong, A.G.L., Mao, P., Tan, K.S.W., Han, J.Y., Lim, C.T., 2010. *Lab Chip* 10, 2605–2613.
- Huang, S., Undisz, A., Diez-Silva, M., Bow, H., Dao, M., Han, J.Y., 2013. *Integr. Biol.-Uk* 5, 414–422.
- Kang, Y.J., Ha, Y.R., Lee, S.J., 2016. *Analyst* 141, 319–330.
- Karl, S., Mueller, I., St Pierre, T.G., 2015. *Nat. Med.* 21, (1387–1387).
- Lange, J.R., Steinwachs, J., Kolb, T., Lautscham, L.A., Harder, I., Whyte, G., Fabry, B., 2015. *Biophys. J.* 109, (661–661).
- Liu, Z.B., Lee, Y., Jang, J.H., Li, Y., Han, X., Yokoi, K., Ferrari, M., Zhou, L.D., Qin, L.D., 2015. *Sci. Rep.-Uk*, 5.
- Makler, M.T., Palmer, C.J., Ager, A.L., 1998. *Ann. Trop. Med. Parasit.* 92, 419–433.
- Mills, J.P., Diez-Silva, M., Quinn, D.J., Dao, M., Lang, M.J., Tan, K.S.W., Lim, C.T., Milon, G., David, P.H., Mercereau-Puijalon, O., Bonnefoy, S., Suresh, S., 2007. *P Natl. Acad. Sci. USA* 104, 9213–9217.
- Molineaux, L., Diebner, H.H., Eichner, M., Collins, W.E., Jeffery, G.M., Dietz, K., 2001. *Parasitology* 122, 379–391.
- Nyberg, K.D., Scott, M.B., Bruce, S.L., Gopinath, A.B., Bikos, D., Mason, T.G., Kim, J.W., Choi, H.S., Rowat, A.C., 2016. *Lab Chip* 16, 3330–3339.
- Otto, O., Rosendahl, P., Mietke, A., Golfier, S., Herold, C., Klaue, D., Girardo, S., Pagliara, S., Ekpenyong, A., Jacobi, A., Wobus, M., Topfner, N., Keyser, U.F., Mansfeld, J., Fischer-Friedrich, E., Guck, J., 2015. *Nat. Methods* 12, 199–202.
- Park, Y.K., Diez-Silva, M., Popescu, G., Lykotrafitis, G., Choi, W.S., Feld, M.S., Suresh, S., 2008. *P Natl. Acad. Sci. USA* 105, 13730–13735.
- Peng, W.K., Kong, T.F., Ng, C.S., Chen, L., Huang, Y.X., Bhagat, A.A.S., Nguyen, N.T., Preiser, P.R., Han, J., 2014. *Nat. Med.* 20, 1069–1073.
- Prescott, W.R., Jordan, R.G., Grobusch, M.P., Chinchilli, V.M., Kleinschmidt, I., Borovsky, J., Plaskow, M., Torrez, M., Mico, M., Schwabe, C., 2012. *Malar. J.* 11, 155.
- Rosenbluth, M.J., Lam, W.A., Fletcher, D.A., 2008. *Lab a Chip* 8, 1062–1070.
- Ross, N.E., Pritchard, C.J., Rubin, D.M., Duse, A.G., 2006. *Med Biol. Eng. Comput.* 44, 427–436.
- Shelby, J.P., White, J., Ganesan, K., Rathod, P.K., Chiu, D.T., 2003. *P Natl. Acad. Sci. USA* 100, 14618–14622.
- Song, H.J., Wang, Y., Rosano, J.M., Prabhakarandian, B., Garson, C., Pant, K., Lai, E., 2013. *Lab a Chip* 13, 2300–2310.
- Tse, H.T.K., Gossett, D.R., Moon, Y.S., Masaeli, M., Sohsman, M., Ying, Y., Mislick, K., Adams, R.P., Rao, J.Y., Di Carlo, D., 2013. *Sci. Transl. Med.* 5.
- Wan, J.D., Ristenpart, W.D., Stone, H.A., 2008. *P Natl. Acad. Sci. USA* 105, 16432–16437.
- Yager, P., Edwards, T., Fu, E., Helton, K., Nelson, K., Tam, M.R., Weigl, B.H., 2006. *Nature* 442, 412–418.
- Zhang, W.J., Kai, K., Choi, D.S., Iwamoto, T., Nguyen, Y.H., Wong, H.L., Landis, M.D., Ueno, N.T., Chang, J., Qin, L.D., 2012. *P Natl. Acad. Sci. USA* 109, 18707–18712.
- Zheng, Y., Shojaei-Baghini, E., Azad, A., Wang, C., Sun, Y., 2012. *Lab Chip* 12, 2560–2567.
- Zheng, Y., Nguyen, J., Wang, C., Sun, Y., 2013. *Lab a Chip* 13, 3275–3283.